Authors: Christeson, GL, Collins, GS, Morgan, JV, Gulick, SPS, Barton, PJ, Warner, MR,

Title: Mantle deformation beneath the Chicxulub impact crater

Journal: Earth and Planetary Science Letters, 2009, Vol: 284, Pages: 249 - 257

DOI: doi:10.1016/j.epsl.2009.04.033

Mantle deformation beneath the Chicxulub impact crater

Gail L. Christeson[1], Gareth S. Collins[2], Joanna V. Morgan[2], Sean P.S. Gulick[1], Penny J. Barton[3], Michael R. Warner[2].

[1]University of Texas Institute for Geophysics, Jackson School of Geosciences, J.J. Pickle Research Campus, Mail Code R2200, 10100 Burnet Rd, Austin, Texas 78758, USA. [2]Department of Earth Science and Engineering, South Kensington Campus, Imperial College, London SW7 2AZ, UK. [3]Bullard Laboratories, Department of Earth Sciences, University of Cambridge, Cambridge CB2 3EQ, UK.

ABSTRACT

The surface expression of impact craters is well-known from visual images of the Moon, Venus, and other planets and planetary bodies, but constraints on deep structure of these craters is largely limited to interpretations of gravity data. Although the gravity models are non-unique, they do suggest that large impact craters are associated with structure at the base of the crust. We use seismic data to map Moho (crust-mantle interface) topography beneath the Chicxulub crater, the youngest and best preserved of the three largest known terrestrial impact craters. The Moho is upwarped by ~1.5-2 km near the center of the Chicxulub crater, and depressed by ~0.5-1.0 km at a distance of ~30-55 km from the crater center. A comparison with numerical modeling results reveal that immediately following impact a transient crater reached a maximum depth of at least 30 km prior to collapse, and that subsequent collapse of the transient crater uplifted target material from deep below the crater floor. These results demonstrate that deformation from large terrestrial impacts can extend to the base of the continental crust. A similar Moho topography is also modeled for some large lunar and Martian craters, which suggests that mantle deformation may play a prominent role in large crater formation.

Keywords: Chicxulub, terrestrial impact, Moho, crater.

1. INTRODUCTION

The morphology of impact craters changes with size, progressing from small simple bowl-shaped craters to large multi-ring craters (e.g., Gilbert, 1893; Dence, 1965; Hartmann, 1972; Schultz, 1976; Wilhelms et al., 1987; Melosh, 1989). The formation of small craters is fairly well understood from terrestrial field studies and laboratory tests, but the construction of large craters is not easily extrapolated from these observations since the kinematics of cratering change with size (e.g., Melosh, 1989). Thus it is essential to obtain constraints on the deep structure of impact craters in order to further our understanding of the formation of large impact craters.

Visual images from the Moon, Venus, and other planets and planetary bodies constrain the surface expression of different crater types, but provide no subsurface information. Gravity data over these craters offer some control on deeper crater structure; however, gravity models are non-unique with trade-offs between density contrasts, interface topographies, and layer thicknesses. Nonetheless, mantle upwarping beneath many large lunar and Martian craters is modeled from gravity data, and has been attributed to rapid mantle uplift following impact (e.g., Wise and Yates, 1970; Neumann et al., 1996; Wieczorek and Phillips, 1998; Neumann et al., 2004; Mohit and Philipps, 2007).

Mantle topography has also been inferred beneath the large terrestrial Chicxulub impact crater. Seismic reflection profiles image crater-related crustal reflectivity that extends to the base of the crust and in places may be associated with faulting at the crust-mantle boundary (Morgan et al., 1997; Morgan and Warner, 1999). Initial modeling of a two-dimensional wide-angle seismic refraction profile collected in 1996 suggested that the Moho may be upwarped at the crater center; however, resolution analyses indicate that a model with no mantle upwarping will also adequately fit these data (Christeson et al., 2001). The timescale of mantle upwarping is inferred to be rapid based on the absence of upwarping and/or thinning of post-impact sediments in the center of the basin.

Here we analyze a more extensive dataset, using all seismic wide-angle data acquired in two separate experiments to produce a well-constrained three-dimensional map of Moho topography beneath the Chicxulub crater. These data show that the Moho is upwarped by ~1.5-2 km near the crater center, and depressed by ~0.5-1.0 km at a distance of ~30-55 km from the crater center. We also compare these results with new numerical models of Chicxulub crater formation. These results demonstrate that deformation from the Chicxulub impact extends to the base of the continental crust.

2. LOCATION AND SEISMIC EXPERIMENT

The 180-200 km diameter Chicxulub structure, located in the northwest Yucatan (Fig. 1), has been previously identified as the crater associated with the 65 Ma Cretaceous-Tertiary impact event (Hildebrand et al., 1991; Sharpton et al., 1992; Swisher et al., 1992). Other large terrestrial impact craters include the 2.02 Ga Vredefort crater in South Africa (250-300 km diameter) and the 1.85 Ga Sudbury crater in Canada (250-300 km diameter) (Grieve and Therriault, 2000). The Vredefort crater has been heavily eroded (Reimold and Gibson, 1996) and the Sudbury crater strongly deformed (Grieve and Therriault, 2000); in comparison the younger Chicxulub crater is relatively pristine owing to burial beneath ~1 km of carbonate rocks (Morgan et al., 1997) and the tectonically quiescent location of the impact site.

The 1996 Chicxulub seismic experiment (Fig. 1) consisted of ~650 km of marine seismic reflection profiles recorded on 34 ocean bottom and 91 land seismometers (Morgan et al., 1997). The 2005 seismic experiment (Fig. 1) acquired ~1500 km of marine seismic reflection profiles which were recorded on 28 ocean bottom and 87 land seismometers (Gulick et al., 2008). Representative record sections that display crustal refractions (*Pg*) and Moho reflections (*PmP*) are shown in Fig. 2. We utilized data from both field programs in our seismic analysis.

3. METHODS

3.1. Crustal velocity structure.

The goal of our seismic analysis is to map topography along the crust-mantle interface (Moho). However, inverting for the Moho interface requires that we first have a well-constrained three-dimensional crustal velocity structure that covers the entire region where instruments and shots are located that recorded *PmP* reflections. We therefore utilized the tomographic method described by Zelt and Barton (1998) to constrain the three-dimensional structure of the region using the first-arrival picks to create a velocity grid . Similar inversions were presented in previous studies (Morgan et al., 2002; Vermeesch and Morgan, 2008; Vermeesch et al., 2009) but these were high-resolution models focused on the crater center; our analysis differs in that shots and receivers from the entire 1996 and 2005 seismic experiment are included and hence the velocity tomogram covers a larger volume (365 x 248 x 40 km) but at a coarser resolution (1-km grid).

We picked all observed *Pg* first-arrival travel times for all seismometers at a 500-m spacing along each shot line. This resulted in a total of ~125,000 first-arrival picks. Our three-dimensional starting velocity model was constructed by linearly interpolating between two-dimensional velocity models previously obtained for profiles Chicx-A/A1 (Christeson et al., 2001), Chicx-B/F (Christeson et al., 2001), and Chicx-C (Brittan et al., 1999). The forward and inverse velocity grid were parameterized at 1.0 km. The tomographic inversion was carried out for ten iterations, and at each iteration three smoothing parameters were tested. The final preferred model was chosen as the iteration that produced the smoothest model with a chi-square value of 1.0 (i.e., the model fits the observed travel-times within their estimated uncertainties which were set to 25 ms for source-receiver offsets <30 km, 50 ms for offsets 30-60 km, and 100 ms for offsets >60 km).

Four slices through the final velocity model are displayed in Fig. 3; plots show velocity anomaly with respect to average velocity for the entire region at each depth. Prominent features include a high-velocity anomaly near the crater center at ~5-10 km depth, a high-velocity region

in the northwest, and a low-velocity region in the northeast. There is little ray coverage below 15-20 km depth, and thus these depths are not constrained by the tomographic inversion.

3.2. Moho interface.

We solved for Moho interface depth using the method presented by Zelt et al. (2003). This technique uses one reflected phase (*PmP*) to invert for one interface (the Moho) with a fixed velocity model. We picked observed *PmP* secondary arrivals for all seismometers at a 500-m spacing along each shot line, and set all pick uncertainties to 125 ms. The crustal velocity model obtained from tomographic inversion of first-arrivals was modified such that velocities were set to 6.65 km/s below 25 km. This modification decouples the first-arrival and reflection tomography inversions and results in an objective estimate of Moho depth (Zelt et al., 2003).

We inverted for both the most horizontal (flattest, Fig. 4a) and most smooth (smoothest, Fig. 4b) interface that fit the data with a chi-square value of 1.0. The resulting inversions are similar, with shallow Moho near the crater center superimposed on a Moho dipping from west to east approximately parallel to the coast. Our preferred model is the flattest Moho (Fig. 4a) because there is less structure at the edges of our ray coverage. We removed a regional trend (Fig. 4c) from the Moho interface and plot the resulting depth anomaly in Fig. 4d. The prominent remaining feature in the Moho topography is an upwarping of 1.5-2.0 km near the crater center, and a deepening of 0.5-1.0 km at a radial distance of ~30-55 km from the center of the Moho upwarping. The interface model is best-resolved within a radius of 75 km of the crater center where ~45,000 reflections from the Moho interface are located.

Our inversion method for Moho interface depth assumes that all misfits between observed and calculated *PmP* travel times results from variability in interface depth. Alternatively, these misfits might arise from variability in crustal velocities at depths not sampled by the first-arrival tomographic inversion (>20 km). We therefore carried out a series of modeling tests to determine the amplitude of crustal velocity anomalies required to reproduce the observed travel times near the crater center. Our background velocity model is that used for the Moho interface inversion. We calculated *PmP* travel times through this model that reflect off the regional Moho interface

(Fig. 4c), and display the difference with the observed travel times in Fig. 5a. The radial distance in this plot is the distance from the approximate center of the modeled Moho upwarping (Fig. 4) at coordinates (-89.51363, 21.36184). The residuals are negative (observed earlier than calculated) at a radial distance of 0 km where the interface model (Fig. 5b) contains Moho upwarping. The best-fitting polynomial through the travel time residuals (red line in Fig. 5a) changes from negative to slightly positive values at ~25 km. We can approximate these residuals with fast crustal velocity anomalies at radial distances of 0-25 km, and slow crustal velocity anomalies at radial distances of 25-45 km. The modeling tests (Fig. 5c-e) indicate that deep crustal velocity anomalies 5-15 km thick with amplitudes of 0.5-1.0 km/s near the crater center can approximate the observed *PmP* travel time misfits. We also estimated the gravity anomaly produced by each of the models in Fig. 5, using the method of Talwani et al. (1959) and assuming a standard relationship for velocity and density (Ludwig et al., 1970). The Moho interface inversion model (Fig. 4a and Fig. 5b) will produce a ~+3 mgal gravity anomaly, while the crustal velocity anomaly models (Figs. 5c-e) will produce anomalies of ~+15-25 mgal; all anomalies have a width of 90-100 km and are positioned near the crater center.

Previous studies (Vermeesch and Morgan, 2008; Vermeesch et al., 2009) conclude that the observed gravity field (Fig. 1) can be adequately reproduced by well-constrained velocity contrasts in the upper 20 km of the crust. For example, the central uplift in the upper crust is associated with a velocity increase of 0.4-0.5 km/s and correlates well with the position of the gravity high located 10-20 km southwest of the crater center. Horizontal velocity variations typically decrease with depth, and thus it is unlikely that velocity anomalies greater than the 0.4-0.5 km/s values observed for the central uplift are present in the deep crust. In addition the calculated 15-25 mgal positive gravity anomaly associated with these 0.5-1.0 km/s anomalies is not observed. Thus we argue that depth changes at the Moho interface are the most realistic source for observed variations in *PmP* travel times.

3.3. Numerical modeling.

Formation of the Chicxulub impact crater has been the subject of many recent two-dimensional numerical modeling studies (e.g., O'Keefe and Ahrens, 1999; Collins et al., 2002; Ivanov and Artemieva, 2002; Ivanov, 2005; Stewart and Senft, 2007; Collins et al., 2008), but none of these studies focused on the agreement between models and observation of Moho deformation. Therefore we performed new numerical modeling calculations to examine the Moho displacement predicted by vertical impact models for a range of impactor sizes.

To simulate the Chicxulub impact we used the iSALE hydrocode (Wünnemann et al., 2006), a multi-material, multi-rheology extension to the SALE hydrocode (Amsden et al., 1980), similar to the SALEB hydrocode (e.g.,Ivanov and Artemieva, 2002; Ivanov, 2005). iSALE includes a constitutive model for geologic materials, developed over several years, that accounts for changes in material shear strength that result from changes in pressure, temperature, and both shear and tensile damage (Melosh et al., 1992; Ivanov et al., 1997; Collins et al., 2004). For large impact crater formation this constitutive model is supplemented by a transient target weakening model, the acoustic fluidization “block-model”, which facilitates deep-seated gravitational collapse of the initial bowl-shaped transient cavity (Melosh and Ivanov, 1999). The thermodynamic behaviour of each material in the model is described by an equation of state (EoS). We used tables generated with the Analytic EoS (ANEOS, Thompson and Lauson, 1972) for dunite to represent the mantle, granite to represent the crust, and calcite to represent the sedimentary sequence. The code is well tested against laboratory experiments at low and high strain-rates (Wünnemann et al., 2006) and other hydrocodes (Pierazzo et al., 2008). Our choices of block-model and other input parameters were based on previous successful models of the Chicxulub impact (Ivanov, 2005; Collins et al., 2008), and are documented in Table 1.

Fig. 6 shows cross-sections through three different vertical impact models at two stages during crater development. The left panels depict the time of maximum transient cavity depth, when the Moho is temporarily depressed downward to the maximum extent; the right panels depict the final crater, when the Moho is uplifted to the maximum extent. The three impact

models differ only in impactor size, which included diameters of 10, 14, and 20 km; in all models the impactor was modeled as a granite sphere with a velocity of 12 km s^{-1}. The target comprised 3-km of sediment, 30-km of crust and a mantle half-space below. In Fig. 6a the transient cavity reaches a maximum depth of 23 km and the width of the mantle depression is <30 km radius; in Fig. 6b the cavity reaches a maximum depth of 30 km and the width of the mantle depression is <50 km radius; in Fig. 6c the cavity reaches a maximum depth of 40 km and the width of the mantle depression is >60 km radius. These models show a correlation between maximum transient cavity depth and radius of mantle depression, with larger transient cavities resulting in a greater radius of observed mantle depression. The models also show that mantle deformation may be present even when the maximum transient cavity depth does not extend to the base of the crust (Figs. 6a-6b).

4. DISCUSSION AND CONCLUSIONS

Our study consists of three components: a tomographic inversion for a crustal velocity model, an inversion for 3-D Moho interface depth beneath the Chicxulub structure, and numerical models to examine the Moho displacement predicted by vertical impact models for a range of impactor sizes. The velocity model is similar to previous analyses (Morgan et al., 2000; Morgan et al., 2002) except that it covers a more extensive offshore region. Increased velocities are observed near the crater center, and are interpreted as 18-20 km of stratigraphic uplift of lower crustal material (Christeson et al., 2001; Morgan et al., 2002). This central uplift is offset from the crater center by ~10-20 km to the west in both the velocity model (Fig. 3) and in the observed gravity field (Hildebrand et al., 2003) (Fig. 1). The velocity model also constrains a high-velocity region in the northwest, and a low-velocity region in the northeast (Fig. 3) which correspond to an observed gravity high and gravity low, respectively (Fig. 1). The northwest high-velocity and high-gravity region has previously been interpreted as shallow basement that was likely a preexisting feature of the Cretaceous basement structure (Christeson et al., 2001).

The northeast low-velocity and low-gravity region is associated with an anomalously deep basin that is interpreted to predate the Chicxulub impact (Gulick et al., 2008).

The prominent feature in the Moho topography is an upwarping of 1.5-2.0 km near the crater center, and a deepening of 0.5-1.0 km at a radial distance of ~30-55 km from the center of the Moho upwarping (Fig. 4). In contrast to the central uplift, the Moho upwarping is not significantly offset from the crater center. If the central uplift and Moho upwarping are related by a common causal mechanism, this implies that uplift of the crater floor (and/or, perhaps, subsequent collapse) occurred in a preferred direction to the WSW. Previous numerical models (e.g., Ivanov and Artemieva, 2002) suggested that the permanent Moho deformation observed in the seismic data is a consequence of temporary downward displacement of the mantle during the formation of a deep transient cavity, followed by rebound and uplift of the mantle directly beneath the transient cavity as it collapses to form the final crater. However, these models show variability in both transient crater depth and the net effect of downward then upward displacement of the Moho. Model parameterizations have included a single-material target (Collins et al., 2002), a two-layer (crust over mantle) target (Ivanov and Artemieva, 2002), and multiple-layer (sediment, crust, mantle) targets (Ivanov, 2005; Collins et al., 2008); the transient crater depth in these models varies from 30-43 km. The Moho topography, or the material at Moho depths for the single layer model, is modeled as: 1) upwarping of ~2-km near the crater center and a deepening of ~2 km between ~5 and 40 km from the crater center (Collins et al., 2002), 2) downwarped to form a concavity with a depth of approximately 2-km and a radius of 50 km (Ivanov and Artemieva, 2002; Ivanov, 2005), or 3) no net displacement directly beneath the crater center, upwarped by ~1 km between 5 and 25 km radial distance, and downwarped by ~1 km between 25 and 45 km radial distance (Collins et al., 2008). No published model of the Chicxulub impact is entirely consistent with the Moho topography imaged by the seismic data, although the simple single-layer model of Collins et al. (2002) provides the best fit to the seismic observations.

To investigate the effect of numerical model assumptions on mantle deformation, and to refine existing models to better match the Moho topography inferred from the seismic data we performed a suite of numerical models similar to those presented by Ivanov (2005) and Collins et al. (2008) using a range of impactor sizes. Our best-fit model (Fig. 6b), which is similar to that of Collins et al. (2008), shows mantle upwarping of ~2-km between the crater center and a radius of ~25 km, surrounded by a deepening of ~1 km between ~25 and 45 km from the crater center. This is in reasonable agreement with the observed mantle deformation at Chicxulub. However, our numerical models also show that the amount of vertical uplift of material beneath the transient crater during collapse is very sensitive to the assumed effective strength of the target, and in particular the difference in effective strength between the crust and mantle. As a consequence of this model sensitivity, the amount of uplift of the Moho beneath the Chicxulub crater may not provide a firm constraint on the size of the transient cavity. This also offers a potential explanation for the variability in net Moho displacement in published models of the Chicxulub impact.

Our new numerical models show that mantle deformation may be present even when the maximum transient cavity depth does not extend to the base of the crust (Figs 6a-6b). Moreover, the models also show a robust correlation between maximum transient cavity depth and radius of mantle depression, with larger transient cavities resulting in a greater radius of observed mantle depression (Fig. 6). Our models are for an impactor striking at a velocity of 12 km s^{-1}. Faster velocities will result in larger transient cavities for a fixed impactor size, but the relationship between maximum transient cavity depth and radius of mantle depression remains the same. Hence the width and amplitude of maximum downwarping of the Moho depends primarily on the maximum depth of the transient cavity, regardless of the exact impact conditions under which the cavity forms (velocity or size of the impactor). The relationship between maximum transient cavity depth and radius of mantle depression is also insensitive to the assumed strength of the crust and mantle; hence, the observed mantle deformation at Chicxulub places a robust constraint on the transient crater depth. The observed mantle downwarping at radial distances

between 30 and 50 km in Fig. 4d implies a maximum cavity depth of at least 30 km. This result, combined with an inferred transient crater diameter of 90-105 km (Morgan et al., 1997), implies a transient crater depth-to-diameter ratio of ~1:3, which is close to the ratio of ~1:2.7 observed in small-scale laboratory experiments and simple craters (e.g, Melosh, 1989). This suggests that the depth-to-diameter ratio is relatively constant for all craters including the large multi-ring Chicxulub impact crater. The fact that the mantle is uplifted at all in the observed Chicxulub Moho demonstrates that collapse of the transient crater must involve deep-seated deformation, and that stratigraphic uplift of rocks beneath large craters must persist to great depths beneath the crater floor. The effective strength of the target beneath the crater immediately after impact must be low enough to allow substantial upward movement of the crater floor before the inwardly collapsing sides of the crater reach the center of the crater, where they would suppress the uplift. This observation may help to distinguish between different styles of crater collapse suggested by numerical models that employ alternative algorithms for reducing the strength of the target during an impact (e.g., Stewart and Senft, 2007).

The structural uplift observed in the upper crust at Chicxulub is offset from the center of the Moho upwarping (Fig. 3); we speculate that uplift of both the Moho and crust are linked and that the asymmetry was produced during the collapse of the transient crater. In other words, we hypothesize that uplift of the crater floor was not exactly vertical, but rather involved a horizontal velocity component in the WSW direction. Whether this asymmetric collapse was a consequence of oblique impact, lateral asymmetry in crustal strength, or random instabilities during crater modification remains an open question. Numerical models of oblique impact suggest that central uplifts do rise with a downrange velocity component (e.g., Ivanov and Artemieva, 2002; Shuvalov and Dypvik, 2004) as suggested by Schultz and d'Hondt (1996). This is supported by geological field evidence for preferred transport direction in central uplifts at eroded terrestrial craters (Scherler et al., 2006; Kenkmann and Poelchau, 2009). Recent numerical models of complex crater formation caused by oblique impact also suggest that, at depth, the central uplift is situated beneath the center of the crater, while at the surface the central

uplift is offset downrange of the crater center (Elbeshausen and Wünnemann, 2008; Wünnemann et al., 2009). Hence, if asymmetric central uplift collapse of the Chicxulub crater is related to the angle and direction of impact, the expected impact direction would be from the ENE. In contrast, remote sensing studies of central peak craters on Venus and the moon show no statistically significant relationship between impact direction and offset of the central uplift from the crater center (Eldholm et al., 1989; Herrick and Forsberg-Taylor, 2003; McDonald et al., 2008). This implies that the asymmetry in crustal and Moho uplifts observed at the Chicxulub crater may not be related to impact direction, but instead may be a consequence of lateral asymmetry in crustal strength, or random instabilities during crater collapse.

Studies of lunar craters reveal Moho topography similar in many ways to that observed at the Chicxulub crater. Modeling of lunar gravity data is non-unique with trade-offs between density contrasts and layer thicknesses, and is further complicated by the fact that crustal thickness is only constrained beneath the Apollo 12 and 14 sites (Toksöz et al., 1974). However, analyses do indicate that physically realistic gravity models require thinned crust beneath most large lunar craters (Neumann et al., 1996; Wieczorek and Phillips, 1998). Direct comparison of mantle deformation beneath lunar and terrestrial craters is complicated by the factor of ~2 difference in crustal thickness and by the factor of ~6 difference in surface gravity. The latter difference implies that impacts of the same mass and velocity will result in a transient crater approximately 6 times larger on the Moon than that formed on Earth (e.g., Holsapple, 1993). Hence, if the Chicxulub transient crater depth was ~30 km, the depth of a transient crater of equivalent scale on the Moon would be ~180 km. Assuming that collapse of the transient crater widens the diameter by the same factor on Earth as it does on the Moon, craters on the Moon may be considered to be crudely equivalent in scale to craters 6 times smaller on Earth (although the final crater depths will be different; see McKinnon et al. (1997)). In other words, Chicxulub may be compared (with caution) to lunar impact basins several hundreds of kilometers across. However, for Chicxulub the pre-impact depth of the crust-mantle boundary (~35 km) was approximately the same as the transient crater depth, whereas the simple scaling arguments

above suggest that for an equivalent-scale lunar crater the depth of the crust-mantle boundary (~60-80 km) would be substantially shallower than the transient crater depth (~180 km). In this case, mantle-uplift beneath the lunar crater would be much greater than that observed at Chicxulub. Hence, substantial thinning of lunar crust beneath large impact basins on the Moon is consistent with the amount of inferred mantle and lower-crustal uplift at Chicxulub based on seismic data.

Crustal thickness models based on lunar gravity data also include an adjacent ring of thickened crust around many craters that lies mainly within the basin rim, but this feature is not as well-constrained and has been suggested to be an artefact of incorrect densities if the region surrounding the basins is extensively brecciated or includes low-density ejecta deposits (Neumann et al., 1996; Wieczorek and Phillips, 1998). However, an upwarped Moho beneath the crater center surrounded by Moho downwarping is a component of models for both the Chicxulub and lunar craters, and this similarity in Moho topography strongly suggests that the ring of thickened crust is a real feature of lunar craters. Moho upwarping has also been modelled beneath some large Martian craters (Neumann et al., 2004; Mohit and Philipps, 2007). These observations from Chicxulub, lunar, and Martian craters suggest that mantle deformation can play a prominent role in large crater formation.

ACKNOWLEDGEMENTS

We are grateful to the captains, crew, and science parties (onshore and offshore) during data acquisition in 1996 and 2005. The modeling work in this paper would not have been possible without the years of model development behind iSALE, for which we are indebted to Kai Wünnemann, Boris Ivanov and Jay Melosh. We thank Linda Elkins-Tanton, John Hole, and 3 anonymous reviewers for their comments which have improved this manuscript. Our work was supported by the National Science Foundation (NSF grants OCE-9415716, OCE-9818868, and OCE-0221101) and the Natural Environmental Research Council. GSC was funded by NERC grant NE/E013589/1. This is UTIG contribution 2068.

REFERENCES CITED

Amsden, A.A., Ruppel, H.M., and Hirt, C.W., 1980, SALE: Simplified ALE Computer Program for Fluid Flow at all Speeds, Los Alamos National Laboratory Report Los Alamos, NM, Los Alamos National Laboratory, p. 101.

Brittan, J., Morgan, J., Warner, M., and Marin, L., 1999, Near-surface seismic expression of the Chicxulub impact crater, *in* Dressler, B.O., and Sharpton, V.L., eds., Large Meteorite Impacts and Planetary Evolution II, Volume Geol. Soc. Am. Spec. Pap. 339, p. 269-279.

Christeson, G.L., Nakamura, Y., Buffler, R.T., Morgan, J., and Warner, M., 2001, Deep crustal structure of the Chicxulub impact crater: Journal of Geophysical Research, v. 106, p. 21751-21769.

Collins, G.S., Melosh, H.J., and Ivanov, B.A., 2004, Modeling damage and deformation in impact simulations: Meteoritics and Planetary Science, v. 39, p. 217-231.

Collins, G.S., Melosh, H.J., Morgan, J.V., and Warner, M.R., 2002, Hydrocode simulations of Chicxulub crater collapse and peak-ring formation: Icarus, v. 157, p. 24-33.

Collins, G.S., Morgan, J.V., Barton, P.J., Christeson, G.L., Gulick, S.P.S., Urrutia-Fucugauchi, J., Warner, M.R., and Wünnemann, K., 2008, Dynamic modeling suggests terrace zone asymmetry in the Chicxulub crater is caused by target heterogeneity: Earth and Planetary Science Letters, v. 270, 221-230, doi.

Dence, M.R., 1965, The extraterrestrial origin of impact craters: Annual New York Academy of Science, v. 123, p. 941-969.

Elbeshausen, D., and Wünnemann, K., 2008, Complex crater formation driven by oblique meteorite impacts, Large Meteorite Impacts and Planetary Evolution IV Conference, p. 3078.

Eldholm, O., Thiede, J., and Taylor, E., 1989, Evolution of the Vøring volcanic margin, Proc. ODP, Sci Results, v. 104, Volume 104: College Station, TX, Ocean Drilling Program, p. 1033-1065.

Gilbert, G.K., 1893, The moon's face: A study of the origin of its features: Bull. Philos. Soc. Wash., v. 12, p. 241-292.

Grieve, R., and Therriault, A., 2000, Vredefort, Sudbury, Chicxulub: Three of a kind?: Annual Review of Earth and Planetary Science, v. 28, p. 305-338.

Gulick, S.P.S., Barton, P.J., Christeson, G.L., Morgan, J.V., McDonald, M., Mendoza-Cervantes, K., Pearson, Z.F., Surendra, A., Urrutia-Fucugauchi, J., Vermeesch, P.M., and Warner, M.R., 2008, Importance of pre-impact crustal structure for the asymmetry of the Chicxulub impact crater: Nature Geosciences, v. 1, p. 131-135.

Hartmann, W.K., 1972, Interplanet variations in scale of crater morphology—Earth, Mars, Moon: Icarus, v. 17, p. 707-713.

Herrick, R.R., and Forsberg-Taylor, N.K., 2003, The shape and appearance of craters formed by oblique impact on the Moon and Venus: Meteoritics and Planetary Science, v. 38, p. 1551-1578.

Hildebrand, A.R., Millar, J.D., Pilkington, M., and Lawton, D.C., 2003, Three dimensional gravity field modelling of the Chicxulub impact crater: Meteoritics & Planetary Science, v. 38 Suppl., p. 150.

Hildebrand, A.R., Penfield, G.T., Kring, D.A., Pilkington, M., Camargo, A., Z., Jacobsen, S.B., and Boynton, W.V., 1991, Chicxulub Crater: A possible Cretaceous/Tertiary boundary impact crater on the Yucatán Peninsula, Mexico: Geology, v. 19, p. 867-871.

383 Holsapple, K.A., 1993, The scaling of impact processes in planetary sciences: Annual Review of
384 Earth and Planetary Science, v. 21, p. 333-373.
385 Ivanov, B.A., 2005, Numerical modeling of the largest terrestrial metorite craters: Solar System
386 Research, v. 39, p. 381-409.
387 Ivanov, B.A., and Artemieva, N.A., 2002, Numerical modeling of the formation of large impact
388 craters, *in* Koeberl, C., and MacLeod, K.G., eds., Catastrophic Events and Mass Extinctions:
389 Impacts and Beyond: Boulder, Colorado, Geological Society of America Special Paper 356,
390 p. 619-630.
391 Ivanov, B.A., Deniem, D., and Neukum, G., 1997, Implementation of dynamic strength models
392 into 2D hydrocodes: Applications for atmospheric breakup and impact cratering.: Int. J.
393 Impact Engineering, v. 20, p. 411-430.
394 Kenkmann, T., and Poelchau, M.H., 2009, Acute-angled collision with Earth: Geology, p. in
395 press.
396 Ludwig, W.J., Nafe, J.E., and Drake, C.L., 1970, Seismic refraction, *in* Maxwell, A.E., ed., The
397 Sea, Vol. 4, Part 1: New York, Wiley-Interscience, p. 53-84.
398 McDonald, M.A., Melosh, H.J., and Gulick, S.P.S., 2008, Oblique impacts and peak ring
399 position: Venus and Chicxulub: Geophysical Research Letters, v. 35, L07203, doi:
400 10.1029/2008GL033346.
401 McKinnon, W.B., Zahnle, K.J., Ivanov, B.A., and Melosh, H.J., 1997, Cratering on Venus:
402 Models and observations, *in* Bougher, S.W., Hunten, D.M., and Phillips, R.J., eds., Venus II:
403 Tucson, Univ. Arizona Press, p. 969-1014.
404 Melosh, H.J., 1989, Impact Cratering: A Geological Process: New York, Oxford Univ. Press,
405 245 p.

406 Melosh, H.J., and Ivanov, B.A., 1999, Impact crater collapse: Annual Review of Earth and
407 Planetary Science, v. 27, p. 385-415.
408 Melosh, H.J., Ryan, E.V., and Asphaug, E., 1992, Dynamic Fragmentation in Impacts:
409 Hydrocode Simulation of Laboratory Impacts: Journal of Geophysical Research, v. 97, p.
410 14735-14759.
411 Mohit, P.S., and Philipps, R.J., 2007, Viscous relaxation on early Mars: A study of ancient
412 impact basins: Geophysical Research Letters, v. 34, L21204, doi: 10.1029/2007GL031252.
413 Morgan, J., and Warner, M., 1999, Chicxulub: The third dimension of a multi-ring impact basin:
414 Geology, v. 27, p. 407-410.
415 Morgan, J., Warner, M., and Chicxulub Working Group, 1997, Size and morphology of the
416 Chicxulub impact crater: Nature, v. 390, p. 472-476.
417 Morgan, J.V., Christeson, G.L., and Zelt, C.A., 2002, Testing the resolution of a 3D velocity
418 tomogram across the Chicxulub crater: Tectonophysics, v. 355, p. 215-226.
419 Morgan, J.V., Warner, M.R., Collins, G.S., Melosh, H.J., and Christeson, G.L., 2000, Peak-ring
420 formation in large impact craters: Geophysical constraints from Chicxulub: Earth and
421 Planetary Science Letters, v. 183, p. 347-354.
422 Neumann, G.A., Zuber, M.T., Smith, D.E., and Lemoine, F.G., 1996, The lunar crust: Global
423 structure and signature of major basins: Journal of Geophysical Research, v. 101, p. 16841-
424 16863.
425 Neumann, G.A., Zuber, M.T., Wieczorek, M.A., McGovern, P.J., Lemoine, F.G., and Smith,
426 D.E., 2004, Crustal structure of Mars from gravity and topography: Journal of Geophysical
427 Research, v. 109, E08002, doi: 10.1029/2004JE002262.

O'Keefe, J.D., and Ahrens, T.J., 1999, Complex craters: Relationship of stratigraphy and rings to impact conditions: Journal of Geophysical Research, v. 104, p. 27091-27104.

Pierazzo, E., Artemieva, N., Asphaug, E., Baldwin, E.C., Cazamias, J., Coker, R., Collins, G.S., Crawford, D., Elbeshausen, D., Holsapple, K.A., Housen, K.R., Korycansky, D.G., and Wünnemann, K., 2008, Validation of numerical codes for impact and explosion cratering: Meteoritics and Planetary Science, p. in press.

Reimold, W.U., and Gibson, R.L., 1996, Geology and evolution of the Vredefort imact structure, South Africa: J. Afr. Earth Sci., v. 23, p. 125-162.

Scherler, D., Kenkmann, T., and Jahn, A., 2006, Structural record of an oblique impact: Earth and Planetary Science Letters, v. 248, p. 43-53.

Schultz, P.H., 1976, Moon morphology : Interpretations based on Lunar Orbiter photography: Austin, University of Texas Press.

Schultz, P.H., and D'Hondt, S., 1996, Cretaceous-Tertiary (Chicxulub) impact angle and its consequences: Geology, v. 24, p. 963-967.

Sharpton, V.L., Dalyrymple, G.B., Marin, L.E., Ryder, G., Schuraytz, B.C., and Urrutia-Fucugauchi, J., 1992, New links between the Chicxulub impact structure and the Cretaceous/Tertiary boundary: Nature, v. 359, p. 819-821.

Shuvalov, V., and Dypvik, H., 2004, Ejecta formation and crater development of the Mjølnir impact: Meteoritics and Planetary Science, v. 39, p. 467-479.

Stewart, S.T., and Senft, L.E., 2007, Frictional melting and complex crater collapse, Bridging the Gap II: Effect of Target Properties on the Impact Cratering Process: Saint-Hubert, Canada, p. Abstract 8021.

Swisher, C.C., III, Grajales-Nishimura, J.M., Montanari, A., Margolis, S.V., Claeys, P., Alvarez, W., Renne, P., Cedillo-Pardo, E., Maurrasse, F.J.-M.R., Curtis, G.H., Smit, J., and McWilliams, M.O., 1992, Coeval $^{40}Ar/^{39}Ar$ ages of 65.0 million years ago from Chicxulub crater melt rock and Cretaceous-Tertiary boundary tektites: Science, v. 257, p. 954-958.

Talwani, M., Worzel, J.L., and Landisman, M., 1959, Rapid gravity computations for two-dimensional bodies with application to the Mendocino submarine fracture zone [Pacific Ocean]: Journal of Geophysical Research, v. 64, p. 49-59.

Thompson, S.L., and Lauson, H.S., 1972, Improvements in the Chart D radiation-hydrodynamic CODE III: Revised analytic equation of state: Albuquerque, N. Mex., USA, Sandia Laboratories, Report SC-RR--71-0714, p. 119.

Toksöz, M.N., Dainty, A.M., Solomon, S.C., and Anderson, K.R., 1974, Structure of the Moon: Reviews of Geophysics, v. 12, p. 539-567.

Vermeesch, P.M., and Morgan, J.V., 2008, Structural uplift beneath the Chicxulub impact structure: Journal of Geophysical Research, v. 113, B07103, doi: 10.1029/2007JB005393.

Vermeesch, P.M., Morgan, J.V., Christeson, G.L., Barton, P.J., and Surendra, A., 2009, Three-dimensional joint inversion of traveltime and gravity data across the Chicxulub impact crater: Journal of Geophysical Research, v. 114, B02105, doi: 10.1029/2008JB005776.

Wieczorek, M.A., and Phillips, R.J., 1998, Potential anomalies on a sphere: Applications to the thickness of the lunar crust: Journal of Geophysical Research, v. 103, p. 1715-1724.

Wilhelms, D.E., McCauley, J.F., and Trask, N.J., 1987, The Geologic History of the Moon: Reston, VA, U.S. Geological Survey Professional Paper 1348.

Wise, D.U., and Yates, M.T., 1970, Mascons as structural relief on a lunar 'Moho': Journal of Geophysical Research, v. 75, p. 261-268.

Wünnemann, K., Collins, G.S., and Melosh, H.J., 2006, A strain-based porosity model for use in hydrocode simulations of impacts and implications for transient crater growth in porous targets: Icarus, v. 180, p. 514-527.

Wünnemann, K., Elbeshausen, D., and Collins, G.S., 2009, Structural evidence for the direction of impact at complex craters: Insight from 3D numerical modeling, 40th Lunar and Planetary Science Conference, p. in press.

Zelt, C.A., and Barton, P.J., 1998, Three-dimensional seismic refraction tomography: A comparison of two methods applied to data from the Faeroe Basin: Journal of Geophysical Research, v. 103, p. 7187-7210.

Zelt, C.A., Sain, K., Naumenko, J.V., and Sawyer, D.S., 2003, Assessment of crustal velocity models using seismic refraction and reflection tomography: Geophysical Journal International, v. 153, p. 609-626.

Table 1 Numerical Model Parameters

Symbol	Definition	Value		
L	Impactor diameter (km)	10, 14, 20		
v_i	Impact velocity (km/s)	12		
ρ_i	Impactor density (kg/m^3)	2680		
T_{dec}	Decay time of acoustic vibrations (s)	100, 140, 200[§]		
$\upsilon_{\lim}$	Kinematic viscosity of acoustically fluidized region ($\times 10^5$ m^2/s)	2, 2.8, 4[§]		
		Mantle	Crust	Sediments
ρ	Reference density (kg/m^3)	3310	2680	2700
Y_0	Cohesion (Yield strength at zero pressure; MPa)	50	50	5
Y_m	von Mises plastic limit (theoretical yield strength at infinite pressure; GPa)	3.5	2.5	0.5
μ_i	Coefficient of internal friction	1.5	1.5	1.0
μ_d	Coefficient of friction (damaged material)	0.6	0.6	0.4
T_m	Melt temperature (ºK)	1436	1673	1500
ξ	Thermal softening parameter	0.7	1.2	1.2
p_{bd}	Brittle-ductile transition pressure (GPa)	3.59	2.59	0.76
p_{bp}	Brittle-plastic transition pressure (GPa)	4.75	3.41	0.92

[§]The decay time of the acoustic vibrations and kinematic viscosity of the fluidized region were assumed to scale proportionally with impactor diameter based on the results of Wünnemann and Ivanov (2003)

Fig. 1. Experiment location; background image is bouguer gravity anomaly map (gravity data courtesy of A. Hildebrand and M. Pilkington). Heavy black line marks the coastline. Black-white dashed and white solid lines indicate the locations of the 1996 and 2005 multichannel seismic profiles, respectively. Circles mark the ocean bottom and land seismometer locations used in our analysis from the 1996 (yellow) and 2005 (maroon) experiments; record sections of marked instruments are displayed in Fig. 2. Inset depicts the regional setting, with red rectangle outlining the region shown in the main location figure.

Fig. 2. Representative record sections; instrument locations are shown in Fig. 1. a) Shots recorded by OBS 01 from Chicx-A/A1 during 1996 experiment; b) Shots recorded by land seismometer D46 from Chicx-A/A1 during 1996 experiment; c) Shots recorded by land seismometer 047 from Chicx-R3 during 2005 experiment. All data have been bandpass filtered with a low cut of 5 Hz and a high cut of 15 Hz. Record sections are plotted with a reduction velocity of 6 km/s, and have a 1.0 second automatic gain control applied. *Pg* and *PmP* arrivals are marked.

Fig. 3. Velocity model slices plotted as anomaly with respect to average velocity at each depth; only regions constrained by ray coverage are shown. a) Slice at 5 km depth; contour interval is 0.1 km/s. Yellow lines mark location of slices plotted in Figs. 3b, 3c, and 3d; heavy dark solid line marks coastline. b) Slice along Chicx-BF profile; c) Slice along Chicx-CE profile; d) Slice approximately parallel with the coastline. Crater center is marked by the star in Fig. 3a, and by distance = 0 in Figs. 3b, 3c, and 3d.

Fig. 4. a) Moho interface with inversion parameterized to solve for flattest interface. Interface is only displayed at reflection points. b) As for Fig. 4a, except inversion parameterized to solve for smoothest interface. c) Dipping interface that represents regional Moho trend. e) Depth anomaly between flattest Moho interface and dipping regional trend.

Fig. 5. Left) Difference between observed and calculated *PmP* travel times for the model displayed in the right panel; data is decimated by a factor of 25 for plotting purposes. Radial distance is measured from the approximate center of the modeled Moho upwarping near the crater center. Red line is a polynomial fit to the errors. Right) a) Regional Moho model (Fig. 4c); profile location is approximately parallel to coastline. b) Moho inversion model (Fig. 4a); profile location is approximately parallel to coastline. c) 5-km-thick velocity anomaly model that can approximate observed *PmP* travel times at most radial distances. d) 10-km-thick velocity anomaly model that can approximate observed *PmP* travel times at most radial distances. e) 15-km-thick velocity anomaly that can approximate observed *PmP* travel times at most radial distances.

Fig. 6. Numerical modeling results. a) 10-km diameter impactor; b) 14-km diameter impactor; c) 20-km diameter impactor. Light gray is sediments, medium gray is crystalline basement, and dark gray is mantle. Left panels display transient cavities at the time of maximum crater depth and the right panels depict the final crater.

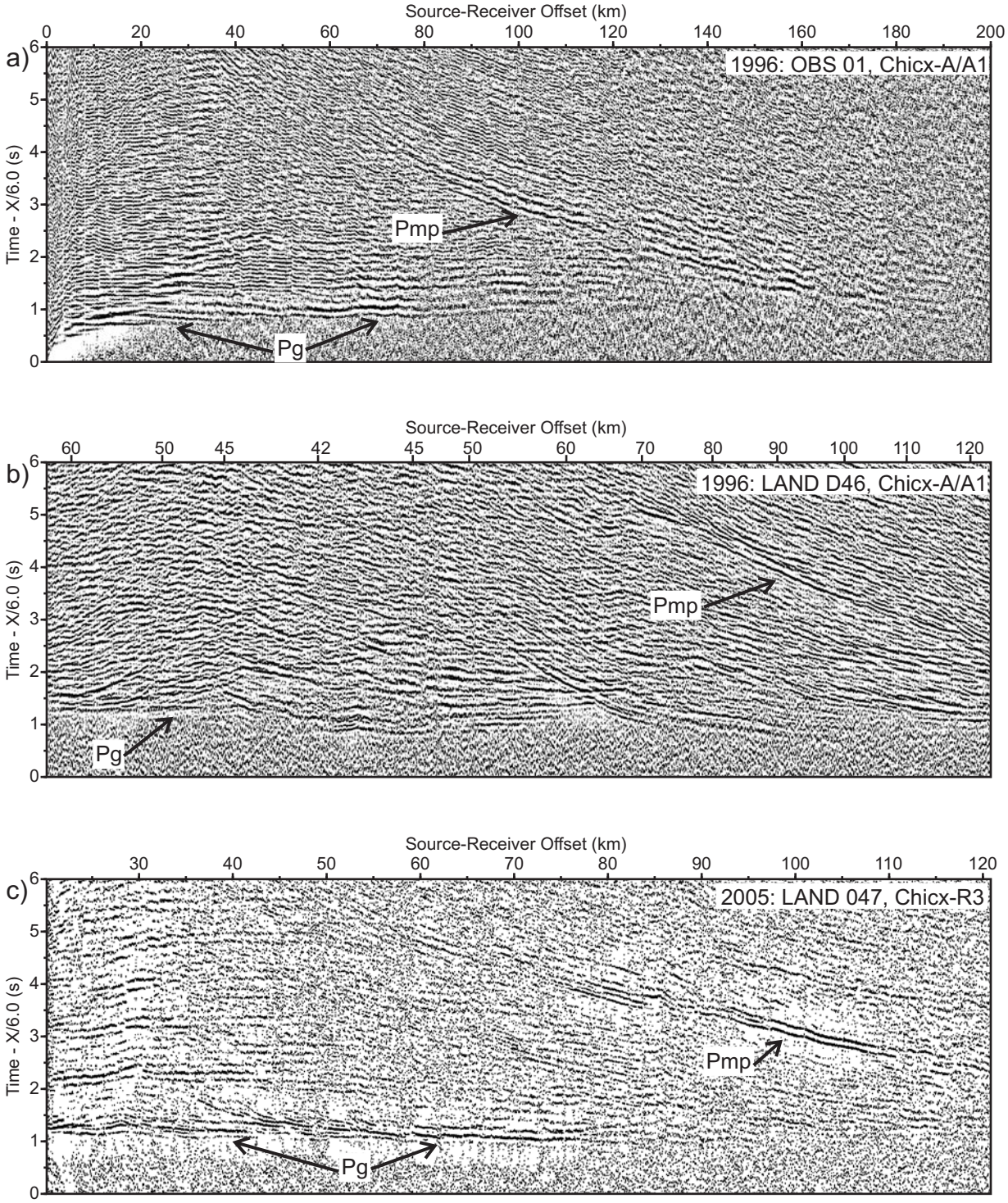
a)
1996: OBS 01, Chicx-A/A1
Source-Receiver Offset (km)
0 20 40 60 80 100 120 140 160 180 200
Time - X/6.0 (s)
0 1 2 3 4 5 6
Pmp
Pg
b)
1996: LAND D46, Chicx-A/A1
Source-Receiver Offset (km)
60 50 45 42 45 50 60 70 80 90 100 110 120
Time - X/6.0 (s)
0 1 2 3 4 5 6
Pmp
Pg
c)
2005: LAND 047, Chicx-R3
Source-Receiver Offset (km)
30 40 50 60 70 80 90 100 110 120
Time - X/6.0 (s)
0 1 2 3 4 5 6
Pmp
Pg

Figure 2

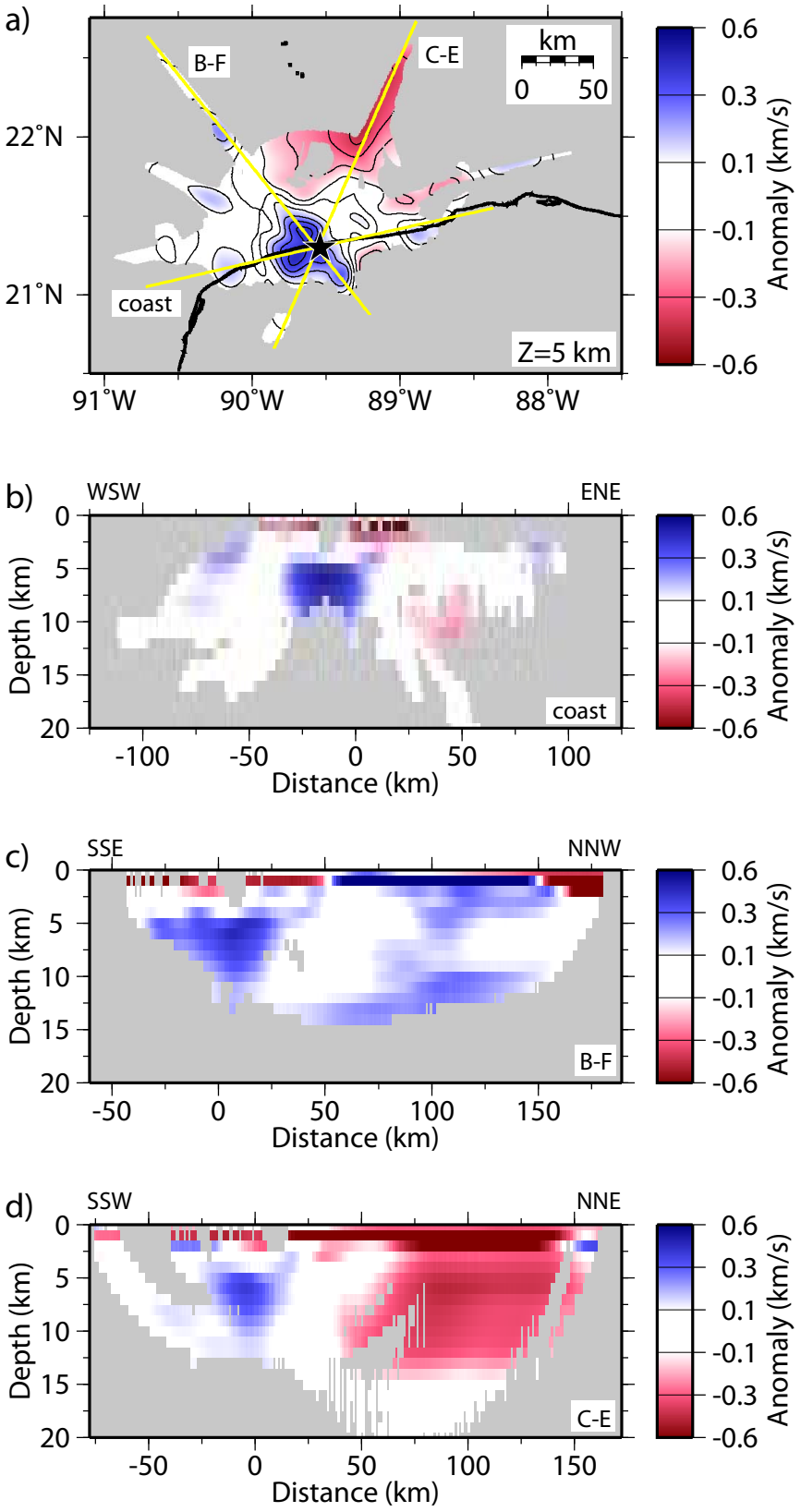
a)
B-F
C-E
km
0 50
22°N
21°N
coast
Z=5 km
91°W
90°W
89°W
88°W
0.6
0.3
0.1
-0.1
-0.3
-0.6
Anomaly (km/s)
b)
WSW
ENE
Depth (km)
0
5
10
15
20
coast
-100
-50
0
50
100
Distance (km)
c)
SSE
NNW
B-F
-50
0
50
100
150
d)
SSW
NNE
C-E

Figure 3

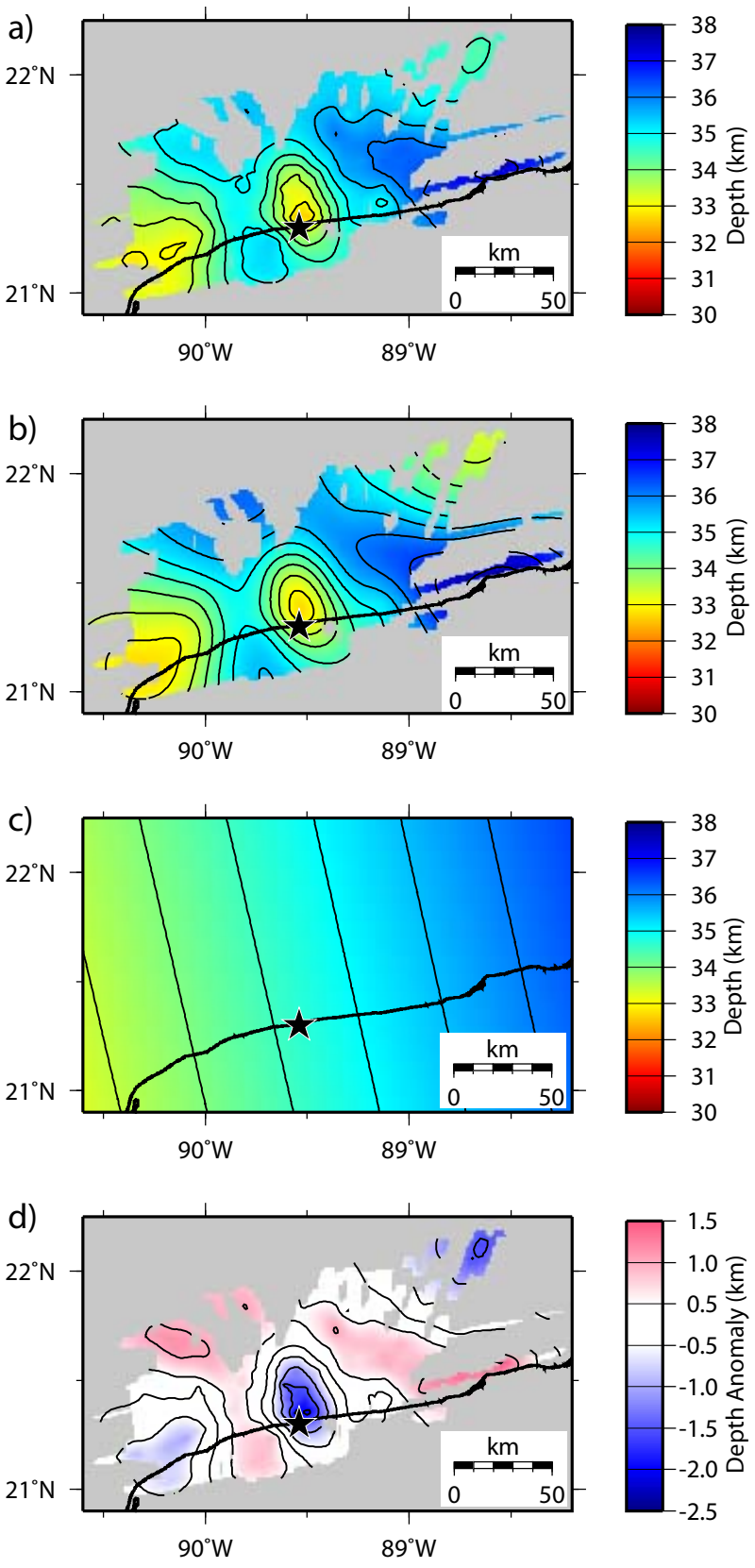
a)
b)
c)
d)
22°N
21°N
90°W
89°W
km
0
50
38
37
36
35
34
33
32
31
30
Depth (km)
1.5
1.0
0.5
-0.5
-1.0
-1.5
-2.0
-2.5
Depth Anomaly (km)

Figure 4

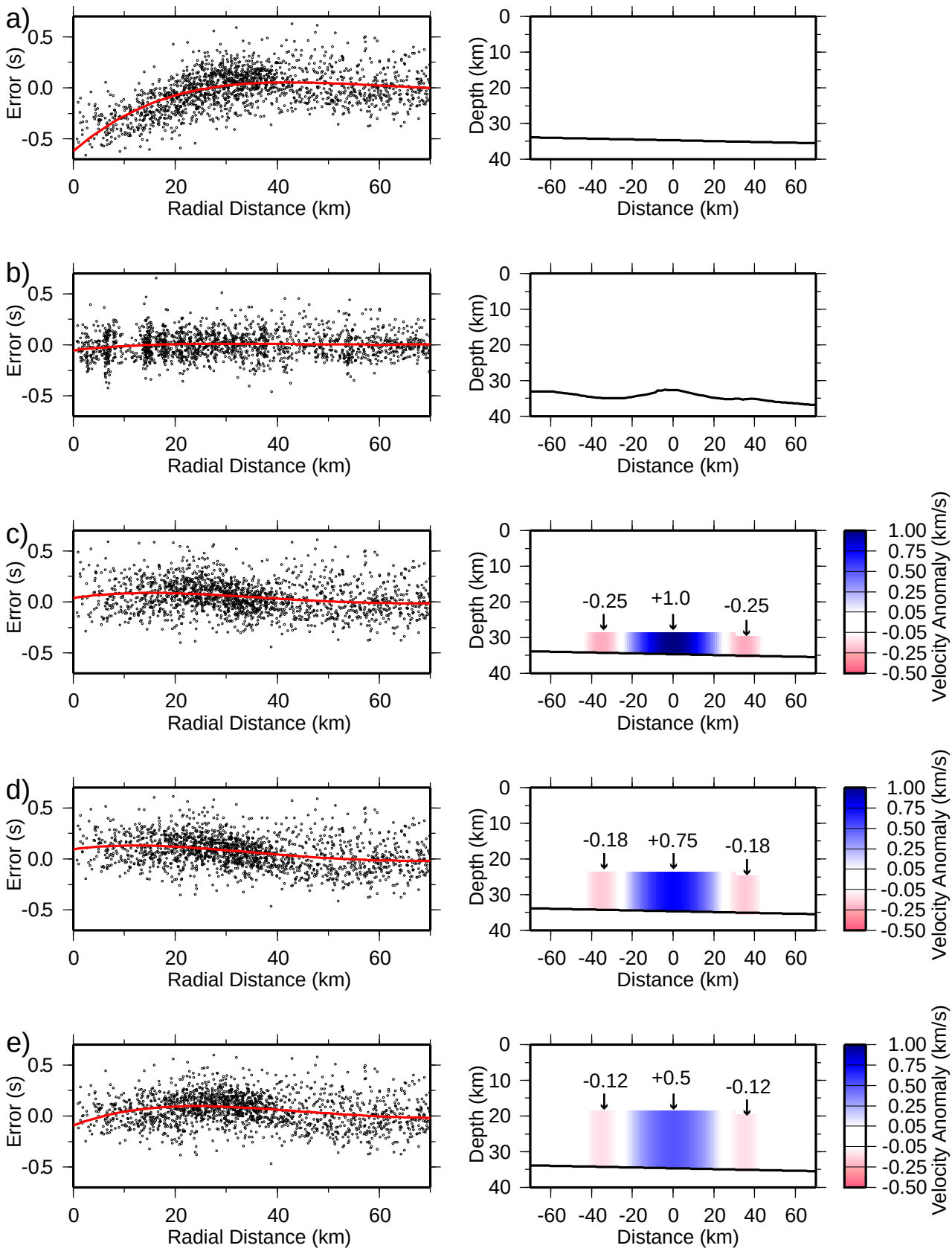
a)
b)
c)
d)
e)
Error (s)
0.5
0.0
-0.5
0
20
40
60
Radial Distance (km)
Depth (km)
0
10
20
30
40
-60 -40 -20 0 20 40 60
Distance (km)
-0.25
+1.0
-0.25
-0.18
+0.75
-0.18
-0.12
+0.5
-0.12
Velocity Anomaly (km/s)
1.00
0.75
0.50
0.25
0.05
-0.05
-0.25
-0.50

Figure 5

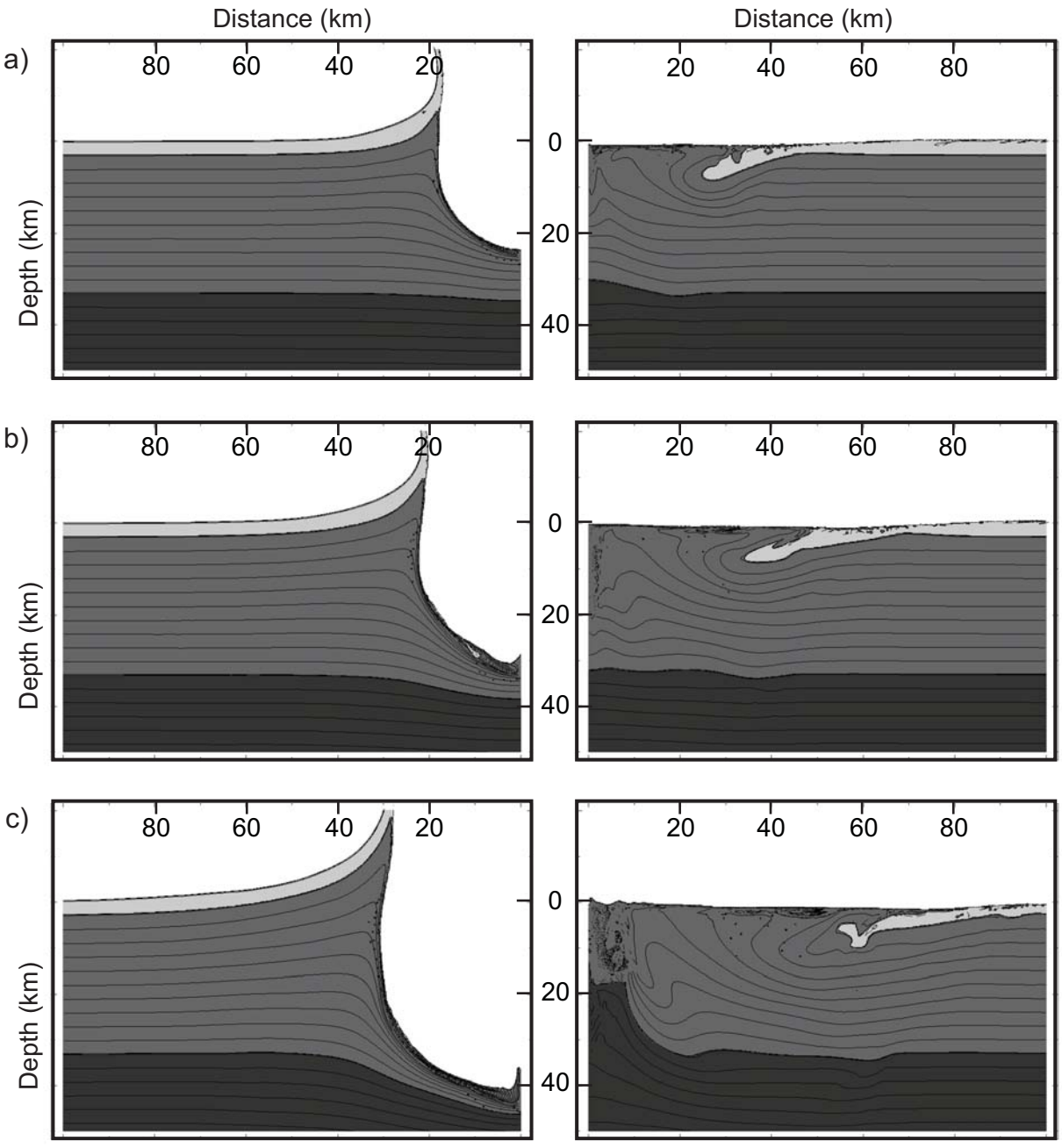
a)
b)
c)
Distance (km)
Distance (km)
80
60
40
20
20
40
60
80
Depth (km)
0
20
40

Figure 6